The solsticial pause on Mars: 1. A planetary wave reanalysis

Lewis, S. R., Mulholland, D. P., Read, P. L., Montabone, L., Wilson, R. J. and Smith, M. D. (2016) The solsticial pause on Mars: 1. A planetary wave reanalysis. Icarus, 264. pp. 456-464. ISSN 0019-1035 doi: 10.1016/j.icarus.2015.08.039 Available at https://centaur.reading.ac.uk/47514/

Icarus 264 (2016) 456–464

Contents lists available at ScienceDirect

Icarus

journal homepage: www.journals.elsevier.com/icarus

The solsticial pause on Mars: 1. A planetary wave reanalysis

Stephen R. Lewis [a,*], David P. Mulholland [b,1], Peter L. Read [b], Luca Montabone [b], R. John Wilson [c], Michael D. Smith [d]

[a] Department of Physical Sciences, The Open University, Walton Hall, Milton Keynes MK7 6AA, UK
[b] Atmospheric, Oceanic & Planetary Physics, University of Oxford, Clarendon Laboratory, Parks Road, Oxford OX1 3PU, UK
[c] Geophysical Fluid Dynamics Laboratory, National Oceanic and Atmospheric Administration, Princeton, NJ 08540-6649, USA
[d] NASA Goddard Space Flight Center, Greenbelt, MD 20771, USA

ARTICLE INFO

Article history:
Received 16 April 2015
Revised 18 August 2015
Accepted 31 August 2015
Available online 15 September 2015

Keywords:
Mars, atmosphere
Mars, climate
Atmospheres, dynamics

ABSTRACT

Large-scale planetary waves are diagnosed from an analysis of profiles retrieved from the Thermal Emission Spectrometer aboard the Mars Global Surveyor spacecraft during its scientific mapping phase. The analysis is conducted by assimilating thermal profiles and total dust opacity retrievals into a Mars global circulation model. Transient waves are largest throughout the northern hemisphere autumn, winter and spring period and almost absent during the summer. The southern hemisphere exhibits generally weaker transient wave behaviour. A striking feature of the low-altitude transient waves in the analysis is that they show a broad subsidiary minimum in amplitude centred on the winter solstice, a period when the thermal contrast between the summer hemisphere and the winter pole is strongest and baroclinic wave activity might be expected to be strong. This behaviour, here called the 'solsticial pause,' is present in every year of the analysis. This strong pause is under-represented in many independent model experiments, which tend to produce relatively uniform baroclinic wave activity throughout the winter. This paper documents and diagnoses the transient wave solsticial pause found in the analysis; a companion paper investigates the origin of the phenomenon in a series of model experiments.

1. Introduction

Planetary wave activity has been observed in the martian winter polar and midlatitude regions in telescopic images and by spacecraft since NASA Mariner 9 and the Viking Landers (e.g. Ryan et al., 1978) and later by Mars Global Surveyor (MGS) (Wilson et al., 2002; Banfield et al., 2004; Hinson and Wang, 2010) and Mars Reconnaissance Orbiter (MRO) (Banfield et al., 2010) amongst others. Waves with periods of 2–7 sols and zonal wavenumbers $s = 1$–4 are typically the most prominent (Barnes, 1980), and amplitudes are much larger in the northern hemisphere (up to 20 K) than in the southern hemisphere (up to 3.5 K) (Banfield et al., 2004). While the largest scale $s = 1$ wave can extend several scale heights above the surface, waves with shorter wavelengths are more confined in the vertical. Several Mars global circulation models (MGCMs) are able to produce waves of broadly similar periods and wavenumbers to those observed (e.g. Barnes et al., 1993; Collins et al., 1996; Wilson et al., 2002).

Whilst wave activity is seen in the northern hemisphere from late summer through to spring, variation in the relative strengths of different zonal wavenumbers has been reported. Banfield et al. (2004) find that $s = 1$ waves dominate around winter solstice, while $s = 2$ and $s = 3$ waves are strongest during autumn and spring. This dominance of the vertically extended $s = 1$ wave at winter solstice ($L_S = 270°$) coincides with a minimum in eddy activity near the surface at this time, a phenomenon known as the 'solsticial pause' (Wang et al., 2005), perhaps first noticed by Barnes (1980) in Viking surface pressure data. This suppression is limited to the lowest 1–2 scale heights of the atmosphere, and transient temperature perturbations above this are seen to reach a maximum around winter solstice (Wang et al., 2005).

Such a suppression, through a reduction in surface windspeed variance and magnitude (Wang et al., 2003), is suspected to exert a strong control over dust lifting along the seasonal polar cap edge. The progression of frontal dust storm frequency in northern midlatitudes has been seen to display a double-peaked structure (Wang, 2007), with a significant reduction in all dust storm activity in the northern hemisphere observed in the later part of a record from $L_S = 170$–$270°$ in three Mars Years (Cantor, 2007). More recently, Guzewich et al. (2015) have identified clear minima at

* Corresponding author.
E-mail address: stephen.lewis@open.ac.uk (S.R. Lewis).
[1] Present address: Department of Meteorology, University of Reading, Harry Pitt Building, Reading RG6 6AL, UK.

http://dx.doi.org/10.1016/j.icarus.2015.08.039
0019-1035/

both solstices in their dust storm climatology based on MGS Mars Observer Camera (MOC) images.

Wang et al. (2013) showed that simulated travelling waves generated significant amounts of energy baroclinically near the surface before and after solstice, but that this generation was greatly reduced at solstice, while eddy kinetic energy was generated barotropically above 30 km throughout the autumn and winter period.

Solsticial minima in transient wave activity of varying amplitudes have been simulated by MGCMs, using prescribed dust distributions representing major dust storm conditions (Hourdin et al., 1995; Kuroda et al., 2007), with more typical prescribed dust loadings (Wilson et al., 2006; Wang et al., 2013; Kavulich et al., 2013), and in an interactive dust-lifting model (Basu et al., 2006). Outside of dust storm conditions, however, modelled reductions to near-surface waves in models have generally not been as dramatic as those observed in the martian atmosphere (e.g. Wang et al., 2005). The reasons for the development of these winter minima, and for their partial representation in MGCMs, have not been fully explored, particularly with regard to the fact that the phenomenon is not restricted to martian years which include a major dust storm (Wang et al., 2005).

This paper documents and diagnoses the transient wave solsticial pause found in a reanalysis (Lewis et al., 2007; Montabone et al., 2006, 2014) of three martian years of Thermal Emission Spectrometer (TES) data (Conrath et al., 2000; Smith et al., 2000; Smith, 2004) into a MGCM. Similar results are found in reanalyses of subsequent years using MCS data, but here we focus on the phenomenon in the most well validated period with data from a single instrument that demonstrates its repeatability in both years with and without a global dust storm. A companion paper (Mulholland et al., 2016) investigates the origin of the phenomenon in a series of independent MGCM experiments.

2. Model and data assimilation

The model used for this study is the UK version of the LMD MGCM developed through a collaboration between groups in France and the UK (Forget et al., 1999; Lewis et al., 1999). The UK version of the model uses a spectral solver for the primitive equations (Hoskins and Simmons, 1975), and employs a semi-Lagrangian advection scheme to transport dust, water vapour, water ice and other tracers (Newman et al., 2002), although tracer transport was not used for the assimilations presented in the present paper, and instead dust was assimilated and updated whenever new observations became available. This is in contrast to the independent model experiments presented in P2. The analyses described here were all carried out using a triangular spectral truncation at total wavenumber 31, corresponding to a $3.75^\circ \times 3.75^\circ$ dynamical grid for nonlinear products and a $5^\circ \times 5^\circ$ physical processes grid, with 25 levels in the vertical between the surface and roughly 100 km altitude.

Data assimilation was conducted using a modified form of the analysis correction scheme (Lorenc et al., 1991), as described in Lewis et al. (2007), using version 2 of the TES retrievals (Smith, 2004) for the scientific mapping period of almost three Mars years (MY) from MY24, $L_S = 141^\circ$ to MY27, $L_S = 72^\circ$ (with updated data and a slightly extended time period from an analysis presented in Montabone et al., 2006). Thermal profiles and total dust opacities from nadir retrievals were assimilated into the model, each centred on the time and place at which they were valid, and model output was stored at two-hourly intervals throughout this period for later analysis. The benefits of data assimilation are that the reanalysis combines information from past and present data and produces physically consistent variables when and where they are not observed. Wave behaviour, in particular, may then be diagnosed more easily using the regularly sampled data set than using the retrievals. All results presented in this paper are taken from this three-year reanalysis (Montabone et al., 2014).

3. The martian solsticial pause

We now describe the martian solsticial pause in wave activity, as represented in the reanalysis. The first subsection describes its temporal form and vertical structure, using longitudinally-averaged data. The following subsection describes the zonal structure of the eddies before during and after the solsticial pause. We then discuss the interannual variability in the phenomenon. Finally, we consider some possible other sources of observational evidence that support this analysis.

3.1. Temporal and vertical structure

Fig. 1 shows the root-mean-square (RMS) variance of atmospheric temperature, 2.5 km above the surface, illustrating clearly the solsticial pause in each of the three years of the assimilation of TES temperature data. The reanalysis data here and in related plots have been bandpass filtered to remove short-period waves, such as the diurnal tide, and any long-period, quasi-stationary waves, retaining only signals with a period within the range 1.5–30 sols. It can be seen that transient eddies are fairly weak (1–3 K) in the midlatitudes of each hemisphere at its winter solstice ($L_S = 90^\circ$ for the southern hemisphere and $L_S = 270^\circ$ for the northern hemisphere), but show peaks in activity either side of solstice, in late autumn and in early spring ($L_S = 0$–60°, 120–180° for the southern hemisphere, $L_S = 180$–240°, 300–360° for the northern hemisphere). This double-peaked structure, with a solsticial pause lasting for at least 60° of L_S in each hemisphere, emerges in each of the three years contained in the reanalysis, and is therefore not reliant on the occurrence of large dust storms (Smith, 2004) during specific periods. Variability in the timing of these events, however, does impart interannual variability to the near-surface eddies, particularly in the northern hemisphere, as discussed later (Section 3.3).

Transient eddy activity is generally stronger, by a factor of about two in terms of RMS air temperature, in the northern hemisphere than in the southern hemisphere: peak RMS values in the northern hemisphere are 7–8 K in each of the three years covered by the assimilation, while southern hemisphere values peak at around 4 K. The regions of peak RMS values in both hemispheres tend to form at higher latitude at the end of summer, move equatorward to mid-latitudes as winter progresses and then reduce in amplitude prior to the winter solstice. Once the eddies have grown again after the solstice, the region of greatest activity returns poleward until the eddies once again reduce in amplitude with the coming of spring. The latitude of the greatest eddy activity broadly follows the latitude of greatest thermal gradient near the surface, coinciding with the edge of the seasonal polar cap.

Fig. 2 illustrates the vertically limited nature of the solsticial pause, focusing on the northern hemisphere (50–70°N). While RMS temperature shows a clear minimum below 300 Pa around $L_S = 270^\circ$ every year, above this, between 100 Pa and 5 Pa, various maxima develop during the period $L_S = 180$–360°. Considerable interannual variability is evident: in MY25, a strong solsticial maximum in variance appears at this level; in the other two years, several shorter maxima form between $L_S \approx 200^\circ$ and $\approx 330^\circ$. These higher-altitude maxima form due to the large meridional temperature gradients that exist in this part of the atmosphere during autumn and winter, as a consequence of the middle atmosphere 'polar warming' (Kuroda et al., 2007; McCleese et al., 2008) (shown

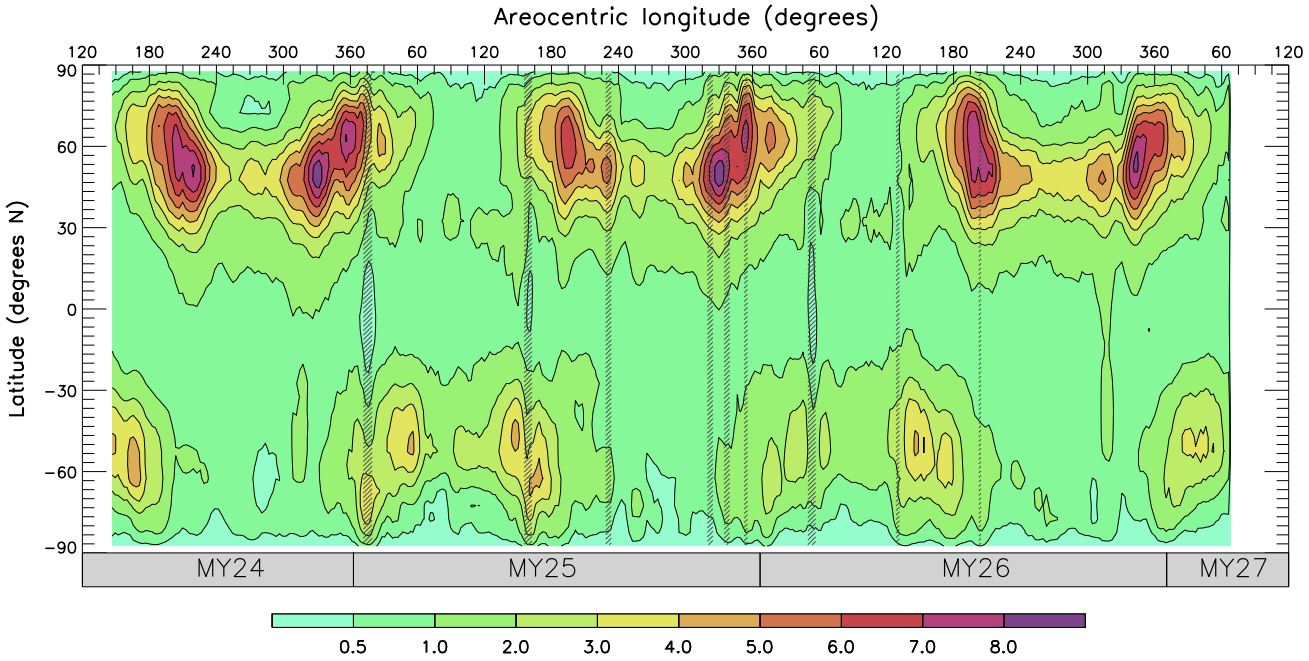

Fig. 1. Root mean-square variance of temperature (K), 2.5 km above the surface, from the TES assimilation dataset, covering approximately three martian years. The variance has been bandpass filtered to include only contributions with periods of 1.5–30 sols; the output is finally smoothed with a 20-sol running mean for clarity. Periods, of one degree of areocentric longitude and longer, during which there are no TES retrievals available and the model continued an independent run are indicated by grey hatching.

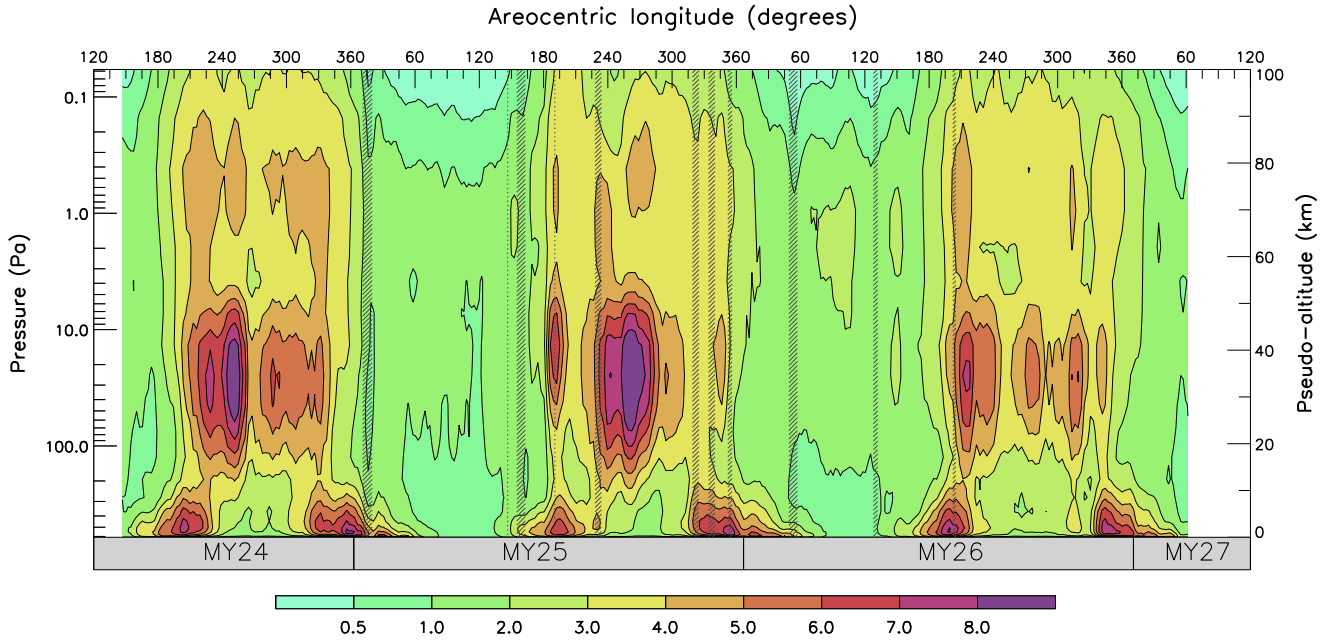

Fig. 2. RMS temperature (K), filtered as in Fig. 1 and with grey hatching indicating the absence of observations, averaged between 50°N and 70°N and plotted as a function of log-pressure, for the full TES assimilation dataset.

later in Fig. 4), and more specifically can be linked to the timing of occurrence of regional and global dust storms (most obviously in MY25, at $L_S = 185°$; also e.g., in MY26, at $L_S = 315°$).

A corresponding figure for a similar latitude range in the southern hemisphere (50–70°S) is presented in Fig. 3. The wave variance is clearly weaker overall, but the solsticial pause is also evident around southern winter solstice ($L_S = 90°$) in each year at low levels in the atmosphere, below about 10 km altitude. There is less evidence of interannual variability in the southern hemisphere than in the northern, most likely related to the fact that the wave activity centres on a time of year ($L_S = 0$–$180°$) when the atmospheric dust loading is also less variable. The most obvious exception is in the middle and upper atmosphere in MY25, at $L_S = 185$–$200°$, in the initial phases of the 2001 global dust storm. There is some evidence that the waves in the lower atmosphere are stronger in southern hemisphere late winter ($L_S = 150$–$180°$) than they are in southern hemisphere early autumn ($L_S = 0$–$30°$) in each of the years in the reanalysis. The longitudinal structure of the southern hemisphere waves in the period when they are strongest will be shown later (Fig. 8).

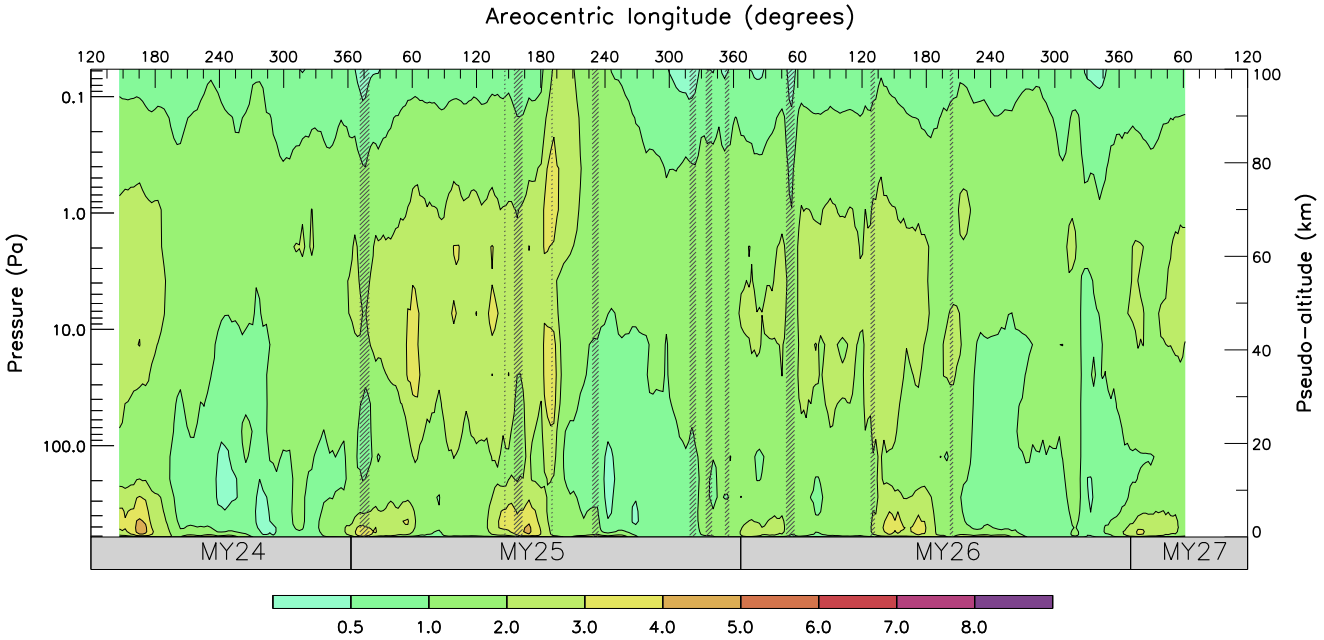

Fig. 3. RMS temperature (K), plotted as in Fig. 2 but for the southern hemisphere, averaged between 50°S and 70°S. The same colour scale is used for consistency. (For interpretation of the references to colour in this figure legend, the reader is referred to the web version of this article.)

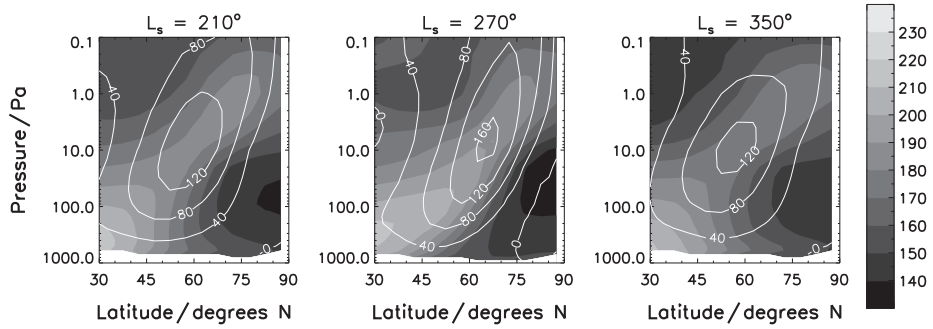

Fig. 4. Zonally-averaged temperature $\overline{T}$ (K, shading) and zonal wind $\bar{u}$ (m s^{-1}, contours) for northern autumn and winter of MY24 of the assimilation. The fields were averaged over 50-sol windows (very roughly 30° of areocentric longitude) centred at L_S = 210° (left), 270° (centre) and 350° (right).

We now consider the vertical and latitudinal structure of the background atmosphere and of the waves in more detail, including the wave heat and momentum fluxes. Fig. 4 shows the state of the atmosphere (again in MY24, in the northern hemisphere) during the pre-solstice maximum (L_S = 210°, left panel), the solsticial minimum (L_S = 270°, centre panel) and post-solstice maximum (L_S = 330°, right panel). An extension of high temperatures into the polar middle atmosphere is observed throughout this period, but is at its strongest at solstice. The westerly jet exhibits a tilt, upward towards the pole, during this northern autumn and winter period. Around solstice, the core of the jet (at 10 Pa) is strengthened and shifted ≈10° to the north (associated with the increase in background dust loading that occurs globally around this time, every year (Haberle et al., 1982; Smith, 2004)), resulting in a greater tilt (away from the vertical) in the lower part of the jet. By late winter (L_S = 330°), the body of the jet has moved back equatorward, its core has weakened and it has regained a homogeneous tilt across its full height.

The structure of the eddies in the northern hemisphere in autumn and winter is shown further in Fig. 5, which may be compared with the mean atmospheric state of Fig. 4, using MY24 as an example (other years are similar). The pre- and post-solstice near-surface eddy maxima are comprised mainly of zonal wavenumbers 2 and 3, with some contribution from wavenumber 1, particularly in the pre-solstice period. The maxima are roughly collocated with the peak zonal-mean meridional temperature gradient, at 45–60°N, but the positions of the maxima move poleward with decreasing wavenumber.

Around solstice, all zonal wavenumbers are weakened near the surface, and the small peaks that remain are shifted southward to ≈ 45°N. $s = 3$ eddies are confined to lower levels throughout, due to constraints on vertical propagation exerted by the zonal-mean flow (Barnes, 1984; Wilson et al., 2002), and the upper-level maxima, which are located on the poleward flank of the jet between 100 Pa and 10 Pa, are comprised almost entirely of eddies with $s \leq 2$.

The transient eddy heat and momentum fluxes shown in Fig. 6 exhibit poleward eddy heat flux, the signature of baroclinic instability, close to the surface before (L_S = 210°) and after (L_S = 350°) solstice. Near solstice, the heat flux and associated baroclinic energy generation near the surface essentially disappears, despite the tightening of the meridional near-surface temperature gradient occurring at this time (Fig. 4). Poleward eddy heat flux peaks at around 10 Pa around solstice, on the poleward jet flank. Eddy momentum fluxes are small near the surface pre- and post-solstice, and are larger at 10 Pa and above, particularly around

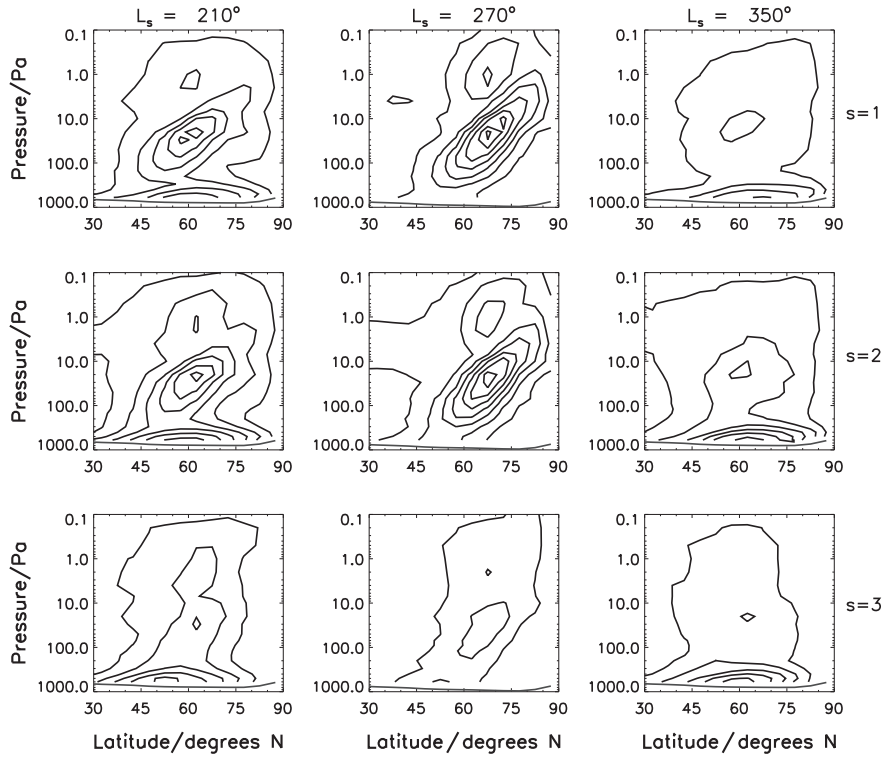

Fig. 5. Zonally averaged RMS temperature from MY24 (in K), filtered as in Fig. 1 and additionally decomposed into zonal wavenumber 1 (top row), 2 (middle row) and 3 (bottom row) components, averaged over 50-sol windows centred at L_S = 210° (left), 270° (centre) and 350° (right). Contours are drawn every 1 K, with the outer (lowest) contour at 1 K in each case.

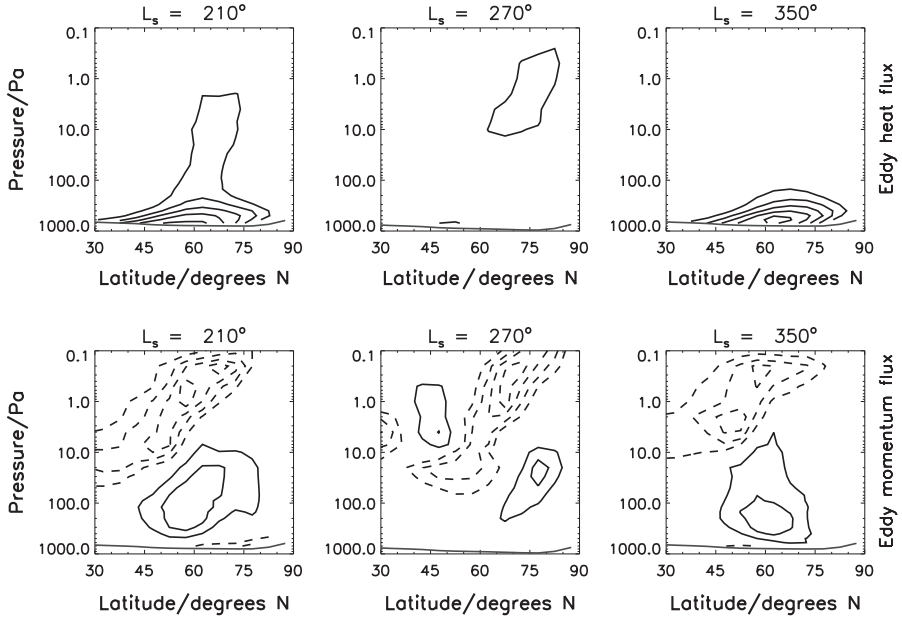

Fig. 6. Transient (1.5–30 sol period) eddy meridional heat (top) and momentum (bottom) fluxes, averaged over 50-sol windows centred at L_S = 210° (left), 270° (centre) and 350° (right) in MY24. Contours are drawn every 10 K m s^{-1} (m^2 s^{-2}), from ±10 to ±50 K m s^{-1} (m^2 s^{-2}), for the heat (momentum) fluxes (excluding the zero contour); negative values are dashed.

solstice, when barotropic generation becomes the larger source of eddy energy in this region of the atmosphere. Integrated over the full height of the atmosphere in the northern extratropics, eddy kinetic energy baroclinic and barotropic generation rates (not shown) are anticorrelated, with a baroclinic (barotropic) minimum (maximum) occurring around solstice.

These results are in good agreement with Wang et al. (2013), who found that MGCM-simulated travelling waves generated significant amounts of energy baroclinically near the surface before and after solstice, but that this generation was greatly reduced at solstice, while eddy kinetic energy was generated barotropically above 30 km throughout the autumn and winter period.

3.2. Zonal structure

The zonal structures of the eddies are now described, using eddy meridional velocity, v, as a measure of the eddy strength rather than temperature as in earlier figures. Zonal modulation is more pronounced in the v field.

The northern mid-latitudes of Mars feature three low-lying areas; Amazonis Planitia, Acidalia Planitia, and Utopia Planitia, centred at longitudes of about −165°E, −20°E, and 120°E respectively. Fig. 7 shows the influence of the three northern plains on eddy behaviour in MY24. The variance in the transient v field is amplified over the low topography. This behaviour is qualitatively similar to that predicted in simulations by Hollingsworth and Barnes (1996), using a model with an older topographic map and a simplified, prescribed dust distribution. The late winter panel ($L_S = 330°$) is also quite similar to Fig. 5 in Wilson et al. (2006), again using a different dust distribution. Banfield et al. (2004) and Wang et al. (2005) have published figures showing temperature variability on a pressure surface, and these also indicate spatial variability with a 'storm track' character. The solsticial pause sees eddies weaken across all longitudes, at latitudes north of ≈ 40°N. Therefore the zonal structure of the eddies in the northern hemisphere can be said to be largely unaffected by the solsticial pause.

Fig. 8, for MY26, shows that eddy activity is much weaker in the southern hemisphere than in the northern. There is strong activity to the south-west of Hellas Planitia (the largest southern hemisphere basin, centred close to 70°E), potentially relevant for the start of global dust events in other years, such as MY25. Several studies (Strausberg et al., 2005; Basu et al., 2006; Cantor, 2007; Martinez-Alvarado et al., 2009) have noted the modulation of winds by travelling waves near Hellas and its possible role in the development of the 2001 global dust storm. The same may be true (Thorpe, 1979), in other years, for the area to the west of Argyre Planitia (the large basin centred near −45°E).

There is a prominent band of relatively strong activity to the west of Argyre, particularly in the $L_S = 130–150°$ period and seen in the $L_S = 150°$ panel of Fig. 8. This was also noted by Hinson and Wilson (2002) and Banfield et al. (2004). Radio science observations (at 67°S) indicate prominent wave activity during the $L_S = 134–162°$ period in MY24, consistent with similar behaviour in MY26 in Fig. 8. The formation of such strong peaks in eddy amplitude appears to be limited to this seasonal window ($L_S \approx 130–180°$), since before (after) this date, with the seasonal polar ice cap edge shifted in latitude, the zone of strongest eddy activity is pushed south (north) of the basin-dominated 40–60°S band (see also Fig. 1). Topographic forcing may therefore be a fundamental component of the solsticial pause in the southern hemisphere in particular.

3.3. Interannual variability

Fig. 9 shows more clearly the interannual variability present in eddy temperature near the surface, both in its total variance and in the dominance of various zonal wavenumbers. Strong, short-lived peaks are particularly evident in $s = 3$ eddies, which often coincide

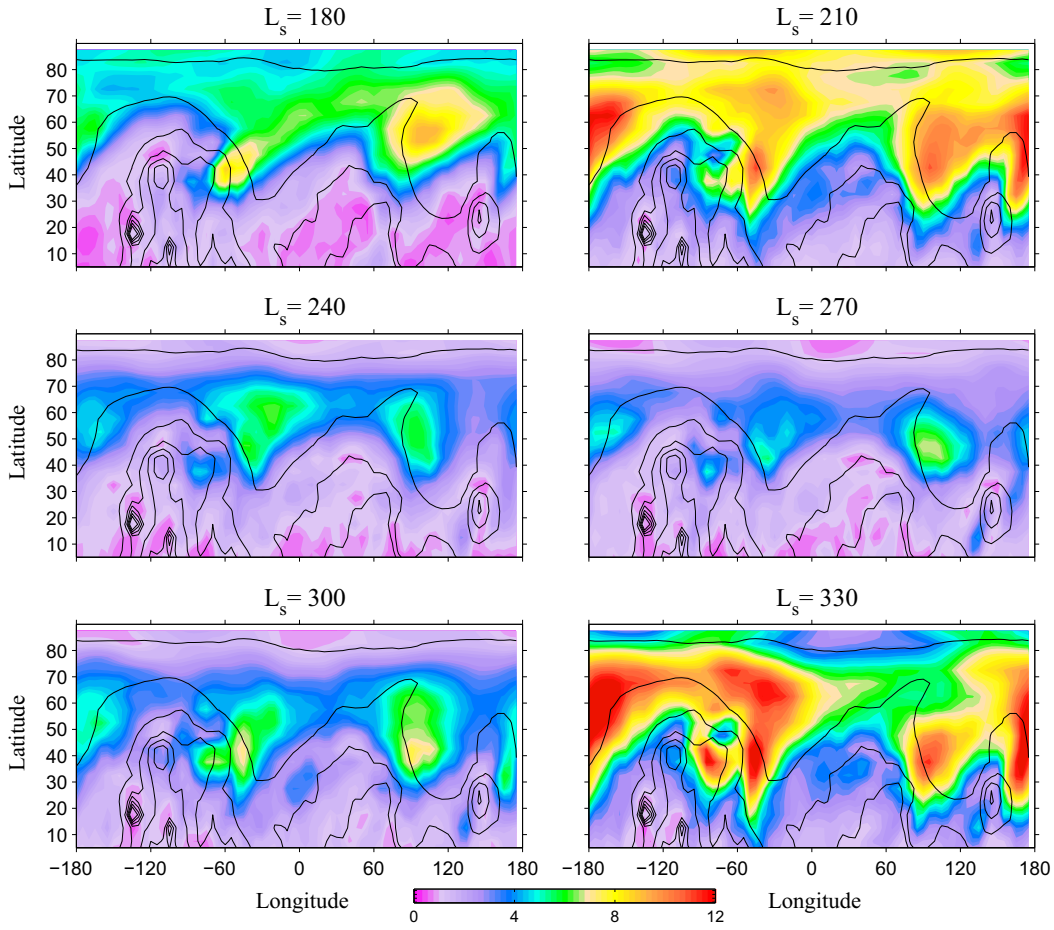

Fig. 7. The spatial distribution of the RMS eddy v field in the northern hemisphere (shaded), for six intervals in MY24. Amplitudes are in m s^{-1}. Contours mark the surface topography. The eddy field is on the 0.83 sigma surface, which corresponds to roughly 1.8 km above ground level. Eddy variance is filtered as in Fig. 1.

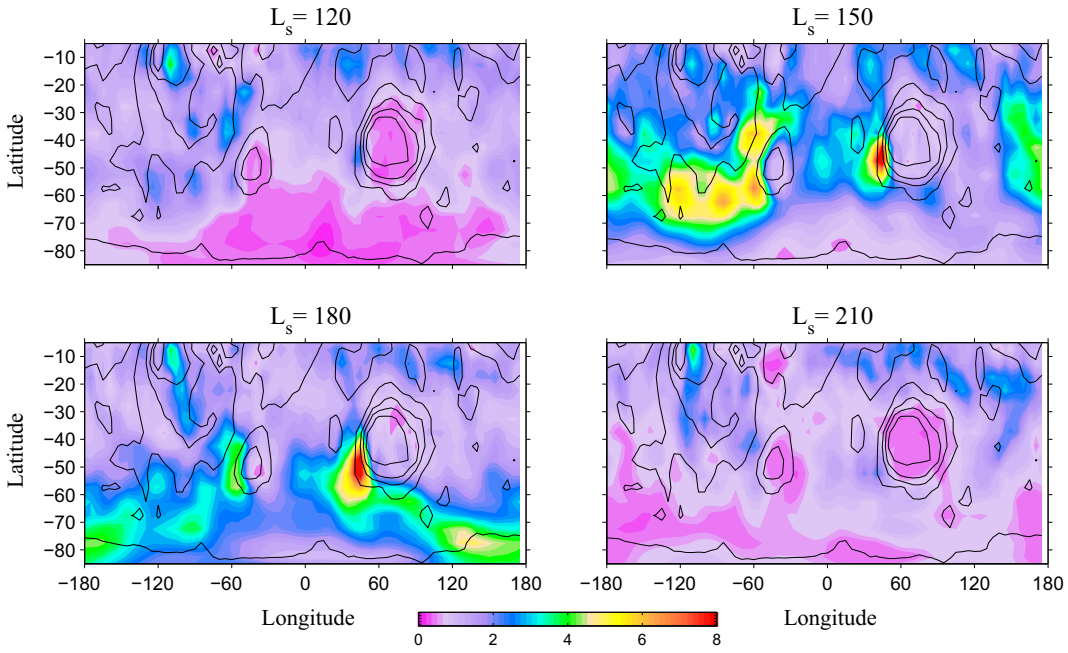

Fig. 8. As for Fig. 7, but for the southern hemisphere, for four intervals in MY26. Note the change in colour axis, reflecting the weaker eddy activity in this season. (For interpretation of the references to colour in this figure legend, the reader is referred to the web version of this article.)

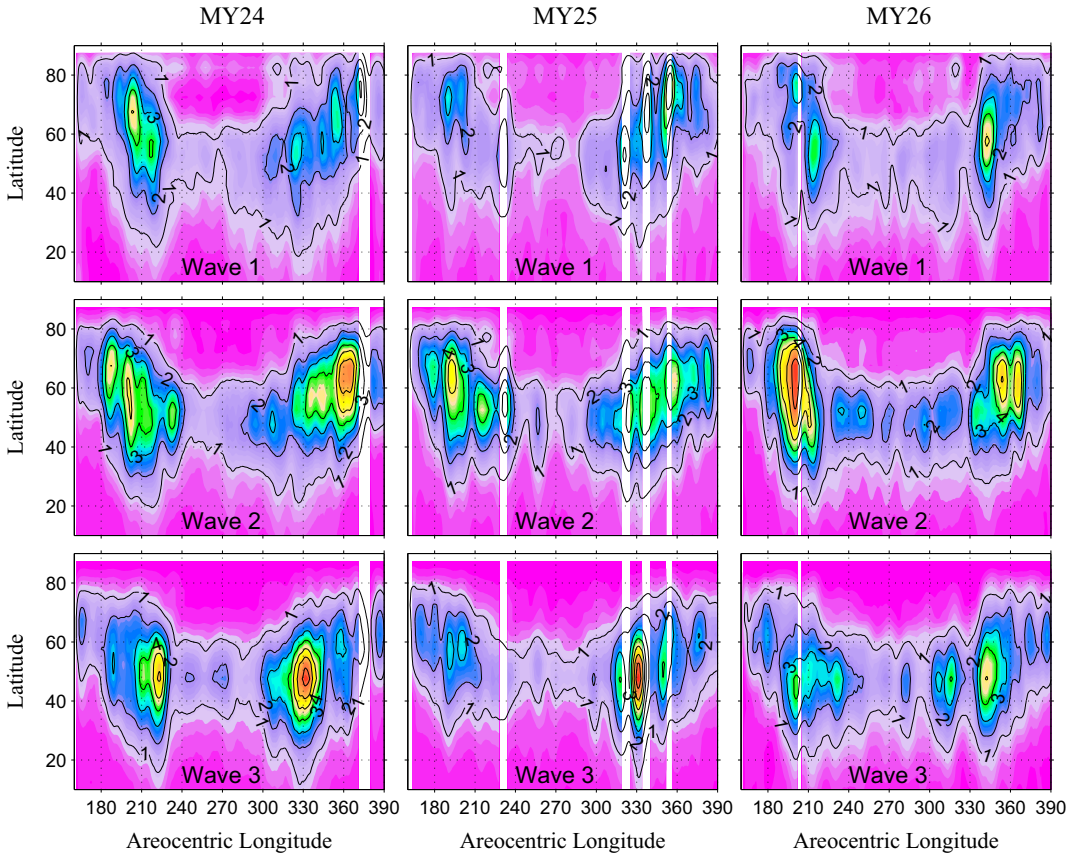

Fig. 9. Seasonal evolution of the RMS eddy *T* field (in K) in the northern hemisphere for MY24 (left column), MY25 (middle column) and MY26 (right column), arranged by contribution from zonal wavenumbers 1, 2 and 3, in the top, middle, and bottom rows, respectively. As in Fig. 7, the eddy field is on the 0.83 sigma surface and filtered as in Fig. 1. Contours are drawn every 1 K, with the outer (lowest) contour at 1 K and shaded for emphasis. The periods during which there are no TES retrievals available are indicated here by an absence of shading.

with local generation of flushing dust storms that grew to regional size (e.g., L_S = 220° in MY24 (Cantor et al., 2001), 325° in MY25 (Wang and Richardson, 2015), 315° in MY26 (Wang, 2007)). Peaks in $s = 2$ tend to form late in the season, after $L_S \approx 330°$, although a particularly large pre-solstice peak occurred in MY26 centred at $\approx 195°$. MY26 was also notable for an unusually early northern hemisphere regional storm beginning at $\approx 185°$ (see Wang and Richardson, 2015 Fig. 2).

The effects of the 2001 global dust storm (which spanned roughly L_S = 180–240°) can be seen in MY25, where eddies appear to be weakened, particularly in the autumn period from L_S = 180° to 230°, in the case of wavenumbers one and three.

As well as being a crucial factor in the generation of flushing dust storms, variability in eddy activity is in turn affected by the increase in global atmospheric opacity and stability that follows the formation of a major dust storm (Wang, 2007), as discussed further in P2 (see their Fig. 14).

The solsticial pause is seen in eddy amplitudes for all zonal wavenumbers, but is most pronounced in $s = 2$ and $s = 3$, owing to the larger maxima that form at these wavenumbers before and after solstice.

3.4. Other observational evidence

Several other sources of observational evidence exist, through which it can be confirmed that the solsticial pause is not unique to the TES reanalysis. Most simply, similar signals in temperature variance were reported by Wang et al. (2005) from a direct analysis of the same TES data used in the assimilation.

Wang et al. (2003) linked the development of flushing storms with the predominance of zonal wavenumbers 2 and 3 within the winter baroclinic region, and attributed the reduced likelihood of these events around solstice with a transition to a dominant $s = 1$ wave occurring at this time. Hinson and Wang (2010) also identified short-period, $s = 3$ waves as being important for flushing storms, and observed numerous transitions between baroclinic modes near the ground in late autumn and early winter of MY27, in MGS radio occultation data, noting that no storms were observed while $s = 1$ was the dominant mode. Our results are broadly consistent with these conclusions. The reanalysis permits all wavenumbers represented in the model to be investigated and we find that the solsticial pause can be attributed to a reduction in the amplitudes of near-surface eddies of all wavenumbers, rather than simply to a shift from shorter wavelengths towards a dominant $s = 1$ mode. In fact, Fig. 9 shows that, at the 0.83 sigma level, $s = 2$ and $s = 3$ are the stronger modes at solstice.

Nonetheless, this link between frontal dust storms and eddy activity means that strong corroborating evidence for the occurrence and regularity of the solsticial pause is available from analysis of dust storm activity, particularly in the northern hemisphere. Wang et al. (2005) performed an analysis of MOC images and found a very clear and abrupt pre-solstice cessation of frontal storms in both MY24 and MY25, with an earlier shut-off date in MY25, at $L_S \approx 205°$ (compared to $L_S \approx 225°$ in MY24), which is consistent with the reduction in eddy activity noted at this time in the previous subsection. The largest of these frontal storms, which move southwards from northern midlatitudes and are known as flushing storms, occurred only during two seasonal windows either side of solstice, and none were observed between $L_S = 240°$ and 300° in MY24 or MY25, or in MY26, when the analysis was continued in Wang (2007). Those flushing storms which progressed beyond the equator occurred just before or after the solsticial minimum, during $L_S \approx 210$—$240°$ in MY24 and MY26, and $L_S \approx 310$—$330°$ in MY25.

Cantor (2007) reported similar results using MOC maps for each of the years MY24-26, focusing on the period $L_S = 170$—$270°$. Further, Cantor et al. (2010), using additional data from MRO, displayed statistics for two full years from late-MY27 to mid-MY29, again showing a clear lack of storm activity between $L_S = 225°$ and $L_S = 300°$. Dust storm frequency over 50–90°N peaked at $L_S \approx 15°$ and again at $L_S \approx 180°$.

Finally, as previously noted, Guzewich et al. (2015) have identified clear minima at both solstices in their multiannual dust climatology, consistent with the timings of the solsticial pause in wave activity observed here, and perhaps a result of reduced dust lifting in the absence of strong, near-surface eddies.

4. Summary and discussion

This paper has demonstrated the existence of a large-amplitude 'solsticial pause' in wave activity on Mars, by using a reanalysis of TES observations over three martian years. The effect is notably more pronounced than that produced in the same model (and in some other models) when run with a prescribed dust scenario (P2). The solsticial pause is robust and is reproduced in each Mars year that is tested. This confirms the ability of assimilation of thermal and dust opacity data to modify the transient baroclinic wave behaviour of a Mars global circulation model in a consistent way, even within a few kilometres of the surface. The solsticial pause occurs in both hemispheres, and at all longitudes, but it is limited to the lowest scale height of the atmosphere. Independent observational evidence is in agreement with the key characteristics of the pause as it appears in the reanalysis.

It is interesting to compare the martian solsticial pause with a terrestrial phenomenon that exhibits some similarities: the reduction in storminess that occurs in midwinter over the northern Pacific ocean, during certain years at a time when linear baroclinic theory predicts a maximum in storminess (Nakamura, 1992). On Earth, the winter midlatitude storm tracks are strongly controlled by the zonal distribution of land and ocean, which leads to a climatological pattern of variance (measured in any of several standard meteorological variables) with maxima over the Pacific and Atlantic oceans, downstream of Eurasia and North America, respectively. While storminess over the Atlantic always peaks in midwinter, during some years the Pacific sector features a solsticial minimum, with a double-peaked pattern in storminess similar to the martian case (e.g. Fig. 1). A range of contributing factors have been suggested, some of which may be applicable to Mars: these include a seasonally-varying diabatic effect, in the form of condensational heating (Chang, 2001), an inverse correlation of wave activity with the strength of the westerly jet (Zhang and Held, 1999), an increase in barotropic damping around midwinter (Deng and Mak, 2006), and a localised reduction in disturbance growth over Asia, possibly caused by the topography present there (Penny et al., 2010; Park et al., 2010).

The longitudinally restricted form of the terrestrial pause makes it quite different to the martian pause, which occurs at all longitudes (Fig. 7). This difference very likely derives from the fundamentally lower level of zonal asymmetry present in the martian midlatitudes, due to the lack of land–sea contrasts. Indeed, some recent studies (e.g., Penny et al., 2010) point to a local, upstream explanation for the Pacific midwinter suppression, whereas the martian solsticial pause is a suppression that occurs throughout the latitude band.

Another important difference between the two is that the terrestrial pause is evident both at the surface and throughout the troposphere (see e.g., Fig. 1 of Nakamura, 1992): in fact, it is strongest at the tropopause level. Although it occupies a similar vertical range, the martian solsticial pause is strongest close to the surface and decays monotonically with height above its maximum (Fig. 2), despite not being confined by a clear tropopause.

A third difference is the regularity of the martian solsticial pause, in contrast to North Pacific storminess, which featured a double-peaked seasonal pattern in only around half of the years studied in Nakamura (1992). These latter two differences may suggest a stronger connection between the pause and the (interannually varying) tropospheric flow on Earth than on Mars, where the solsticial pause, occurring near the surface, appears to be more closely linked to topographic variations and to the occurrence of dust storms.

A companion paper (P2) explores further the factors that contribute to the martian solsticial pause, and seeks to understand the reasons for the difference in the representation of the pause by the UK version of the LMD MGCM in its assimilation and free-running modes.

Acknowledgments

The authors are grateful to two anonymous reviewers for their constructive input. SRL, DPM, and PLR thank the UK Science and Technology Facilities Council and the UK Space Agency for funding, including under Grants ST/J001597/1, ST/I003096/1 and ST/K00106X/1.

References

Banfield, D. et al., 2004. Traveling waves in the martian atmosphere from MGS TES nadir data. Icarus 170, 365–403.
Banfield, D.J. et al., 2010. Forced and traveling waves in MRO MCS atmospheric temperature retrievals. In: 2010 Fall Meeting, AGU, San Francisco, Calif., 13–17 December.
Barnes, J.R., 1980. Time spectral analysis of mid-latitude disturbances in the martian atmosphere. J. Atmos. Sci. 37, 2002–2015.
Barnes, J.R., 1984. Linear baroclinic instability in the martian atmosphere. J. Atmos. Sci. 41, 1536–1550.
Barnes, J.R. et al., 1993. Mars atmospheric dynamics as simulated by the NASA/Ames general circulation model. 2. Transient baroclinic eddies. J. Geophys. Res. 98 (E2), 3125–3148.
Basu, S. et al., 2006. Simulation of spontaneous and variable global dust storms with the GFDL Mars GCM. J. Geophys. Res. E: Planets 111 (9), 1–33, E09004.
Cantor, B.A., 2007. MOC observations of the 2001 Mars planet-encircling dust storm. Icarus 186, 60–96.
Cantor, B.A. et al., 2001. Martian dust storms: 1999 Mars Orbiter Camera observations. J. Geophys. Res. 106, 23653–23687.
Cantor, B.A., James, P.B., Calvin, W.M., 2010. MARCI and MOC observations of the atmosphere and surface cap in the north polar region of Mars. Icarus 208 (1), 61–81.
Chang, E.K.M., 2001. GCM and observational diagnoses of the seasonal and interannual variations of the Pacific storm track during the cool season. J. Atmos. Sci. 58 (13), 1784–1800.
Collins, M. et al., 1996. Baroclinic wave transitions in the martian atmosphere. Icarus 120, 344–357.
Conrath, B.J. et al., 2000. Mars Global Surveyor Thermal Emission Spectrometer (TES) observations: Atmospheric temperatures during aerobraking and science phasing. J. Geophys. Res. 105 (E4), 9509–9519.
Deng, Y., Mak, M., 2006. Nature of the differences in the intraseasonal variability of the Pacific and Atlantic storm tracks: A diagnostic study. J. Atmos. Sci. 63 (10), 2602–2615.
Forget, F. et al., 1999. Improved general circulation models of the martian atmosphere from the surface to above 80 km. J. Geophys. Res. 104 (E10), 24155–24176.
Guzewich, S.D. et al., 2015. Mars Orbiter Camera climatology of textured dust storms. Icarus 258, 1–13, ISSN 0019-103.
Haberle, R.M., Leovy, C.B., Pollack, J.B., 1982. Some effects of global dust storms on the atmospheric circulation of Mars. Icarus 50 (2), 322–367.
Hinson, D.P., Wang, H., 2010. Further observations of regional dust storms and baroclinic eddies in the northern hemisphere of Mars. Icarus 206 (1), 290–305.
Hinson, D.P., Wilson, R.J., 2002. Transient eddies in the southern hemisphere of Mars. Geophys. Res. Lett. 29. http://dx.doi.org/10.1029/2001GL014103.
Hollingsworth, J.L., Barnes, J.R., 1996. Forced stationary planetary waves in Mars's winter atmosphere. J. Atmos. Sci. 53, 428–448.
Hoskins, B.J., Simmons, A.J., 1975. A multi-layer spectral model and the semi-implicit method. Quart. J. R. Meteor. Soc. 101, 637–655.
Hourdin, F., Forget, F., Talagrand, O., 1995. The sensitivity of the martian surface pressure to various parameters: A comparison between numerical simulations and Viking observations. J. Geophys. Res. 100, 5501–5523.
Kavulich Jr., M.J. et al., 2013. Local dynamics of baroclinic waves in the martian atmosphere. J. Atmos. Sci. 70 (11), 3415–3447.
Kuroda, T. et al., 2007. Seasonal changes of the baroclinic wave activity in the northern hemisphere of Mars simulated with a GCM. Geophys. Res. Lett. 34 (9), 1–6, L09203.
Lewis, S.R. et al., 1999. A climate database for Mars. J. Geophys. Res. 104 (E10), 24177–24194.
Lewis, S.R. et al., 2007. Assimilation of Thermal Emission Spectrometer atmospheric data during the Mars Global Surveyor aerobraking period. Icarus 192 (2), 327–347.
Lorenc, A.C., Bell, R.S., Macpherson, B., 1991. The meteorological office analysis correction data assimilation scheme. Quart. J. R. Meteor. Soc. 117, 59–89.
Martinez-Alvarado, O. et al., 2009. Transient teleconnection event at the onset of a planet-encircling dust storm on Mars. Ann. Geophys. 27 (9), 3663–3676.
McCleese, D.J. et al., 2008. Intense polar temperature inversion in the middle atmosphere on Mars. Nat. Geosci. 1, 745–749.
Montabone, L. et al., 2006. Validation of martian meteorological data assimilation for MGS/TES using radio occultation measurements. Icarus 185 (1), 113–132.
Montabone, L. et al., 2014. The Mars Analysis Correction Data Assimilation (MACDA) Dataset V1.0. Geosci. Data J. 1 (2), 129–139.
Mulholland, D.P. et al., 2016. The solsticial pause on Mars: 2 Modelling and investigation of causes. Icarus 264, 465–477.
Nakamura, H., 1992. Midwinter suppression of baroclinic wave activity in the Pacific. J. Atmos. Sci. 49 (17), 1629–1642.
Newman, C.E. et al., 2002. Modeling the martian dust cycle, 1. Representations of dust transport processes. J. Geophys. Res. 107 (E12). http://dx.doi.org/10.1029/2002JE001910.
Park, H.-S., Chiang, J.C.H., Son, S.-W., 2010. The role of the central Asian mountains on the midwinter suppression of North Pacific storminess. J. Atmos. Sci. 67 (11), 3706–3720.
Penny, S., Roe, G.H., Battisti, D.S., 2010. The source of the midwinter suppression in storminess over the North Pacific. J. Clim. 23 (3), 634–648.
Ryan, J.A. et al., 1978. Mars meteorology: Three seasons at the surface. Geophys. Res. Lett. 5, 715–718.
Smith, M.D., 2004. Interannual variability in TES atmopsheric observations of Mars during 1999–2003. Icarus 167, 148–165.
Smith, M.D. et al., 2000. Mars Global Surveyor Thermal Emission Spectrometer (TES) observations of dust opacity during aerobraking and science phasing. J. Geophys. Res. 105 (E4), 9539–9552.
Strausberg, M.J. et al., 2005. Observations of the initiation and evolution of the 2001 Mars global dust storm. J. Geophys. Res.: Planets 110 (E2), E02006.
Thorpe, T.E., 1979. A history of Mars atmospheric opacity in the southern hemisphere during the Viking extended mission. J. Geophys. Res. 84, 6663–6683.
Wang, H., 2007. Dust storms originating in the northern hemisphere during the third mapping year of Mars Global Surveyor. Icarus 189 (2), 325–343.
Wang, H., Richardson, M.I., 2015. The origin, evolution, and trajectory of large dust storms on Mars during Mars years 24–30 (1999–2011). Icarus 251, 112–127.
Wang, H. et al., 2003. Cyclones, tides, and the origin of a cross-equatorial dust storm on Mars. Geophys. Res. Lett. 30 (9) (41-1).
Wang, H., Zurek, R.W., Richardson, M.I., 2005. Relationship between frontal dust storms and transient eddy activity in the northern hemisphere of Mars as observed by Mars Global Surveyor. J. Geophys. Res. E: Planets 110 (7), 1–20.
Wang, H. et al., 2013. Zonal wavenumber three traveling waves in the northern hemisphere of Mars simulated with a general circulation model. Icarus 223 (2), 654–676.
Wilson, R.J. et al., 2002. Traveling waves in the northern hemisphere of Mars. Geophys. Res. Lett. 29 (14), 10.1029/2002GL01486.
Wilson, R.J., Hinson David, Smith, Michael D., 2006. GCM simulations of transient eddies and frontal systems in the martian atmosphere. In: Mars Atmosphere Modelling and Observations, pp. 154–7.
Zhang, Y., Held, I.M., 1999. A linear stochastic model of a GCM's midlatitude storm tracks. J. Atmos. Sci. 56 (19), 3416–3435.